Chapter 3

Nuclear Resonant Spectroscopy of $(Mg_{0.06}Fe_{0.94})O$ at high pressure with in-situ X-ray Diffraction

3.1 Introduction

In Chapter 3, we established that iron-rich magnesium oxide ($X_{Fe} = 0.84$) is characterized by very low sound velocities, and found that a magnetic transition occurred between 15 and 28 GPa.

In this chapter, we present a similar study on a different composition, $(Mg_{0.06}Fe_{0.94})O$, hereafter referred to occasionally as Mw94. In addition to providing insight into the compositional dependence of sound velocities, this chapter also reflects improvements in the methodology since the publication of the previous work. Most notably, availability of in-situ XRD allowed us to directly measure the sample's volume, and thus provide in-situ density (ρ) of our sample for every nuclear resonant scattering (NRS) measurement. This allows us to report the direct result of our NRIXS studies: the Debye sound velocity (V_D) at in-situ ρ. Finally, volumes of this material at room temperature measured as part of a synchrotron Mössbauer study (this chapter) and a thermal equation of state study (Chapter 4) give us an equation of state that is used to convert Debye velocities into compressional and shear wave speeds reliably.

Another direct result of this study is the transition pressure of the paramagnetic to antiferromagnetic transition, also known as the Néel transition (*Fujii et al.*, 2011, e.g.). Mössbauer and magnetic investigations have shown a compositional dependence in Néel temperature in the (Mg,Fe)O solid solution, where projected transition pressure at 300 K coincides with the cubic to rhombohedral distortion (*Speziale et al.*, 2005; *Fujii et al.*, 2011). Other experimental studies, however, find that structural and magnetic transition pressures or temperatures do not coincide (*Kantor et al.*, 2004, 2005, 2006; *Glazyrin et al.*, 2011).

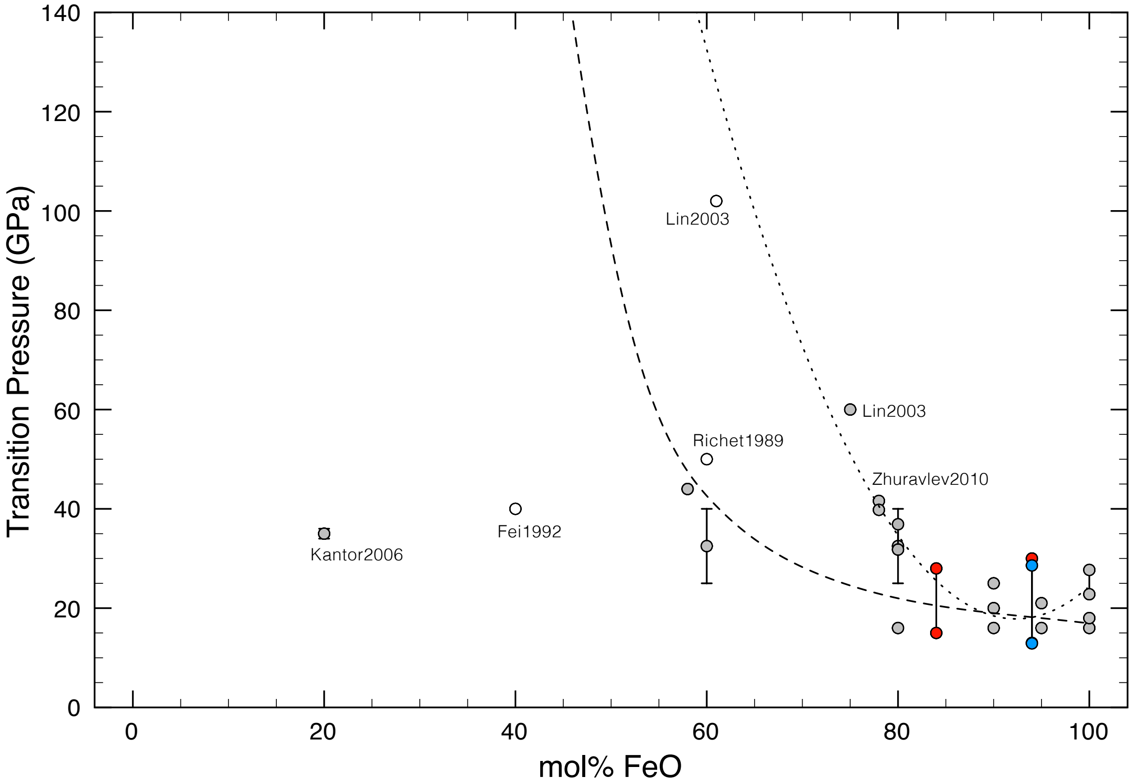

Figure 3.1: Cubic to rhombohedral transition pressures in the literature, as a function of composition. In red we plot our brackets on the magnetic transition pressure from synchrotron Mössbauer spectroscopy of $(Mg_{0.16}Fe_{0.84})O$ (Chapter 2) and $(Mg_{0.06}Fe_{0.94})O$ (this Chapter). In blue we plot the constraint on the cubic to rhombohedral structural transition from X-ray diffraction (Chapter 4). The dashed line indicates the cubic-rhombohedral phase boundary according to *Fei et al.* (2007a), and the dotted line indicates the same according to (*Lin et al.*, 2003). Gray-filled circles are reported transition pressures in the literature (*Mao et al.*, 2002; *Jacobsen et al.*, 2005; *Fei and Mao*, 1994; *Yagi et al.*, 1985; *Zhuravlev et al.*, 2010; *Lin et al.*, 2003; *Shu et al.*, 1998a; *Fei et al.*, 2007a; *Kondo et al.*, 2004; *Richet et al.*, 1989; *Fei et al.*, 2007a; *Kantor et al.*, 2006; *Mao et al.*, 1996), whereas white-filled circles indicate maximum pressures of studies that did not see a transition (*Fei et al.*, 1992; *Richet et al.*, 1989; *Lin et al.*, 2003).

Experimental investigations of the structural transition find that increasing FeO component corresponds to a decrease in transition pressure (*Lin et al.*, 2003; *Shu et al.*, 1998b). The transition pressure is found to be very sensitive to hydrostaticity *Shu et al.* (1998a), and some studies found no compositional dependence of transition pressure (*Kondo et al.*, 2004). Figure 3.1 shows a summary of cubic to rhombohedral structural transition pressures in the literature, which may reflect a compositional dependence. We include our magnetic transition bounds for $(\mathrm{Mg}_{0.16}\mathrm{Fe}_{0.84})\mathrm{O}$ (Chapter 2) and $(\mathrm{Mg}_{0.06}\mathrm{Fe}_{0.94})\mathrm{O}$ (this Chapter), in addition to structural transition constraints for $(\mathrm{Mg}_{0.06}\mathrm{Fe}_{0.94})\mathrm{O}$ (Chapter 4).

We will describe a synchrotron Mössbauer (SMS) study of $(\mathrm{Mg}_{0.06}\mathrm{Fe}_{0.94})\mathrm{O}$ over the pressure range 8 to 52 GPa with in-situ X-ray diffraction. Next, we will describe nuclear resonant inelastic X-ray scattering (NRIXS) measurements over the pressure range 0 to 80 GPa, also taken with in-situ SMS and X-ray diffraction. These results will be compared to an iron-poor sample, $(\mathrm{Mg}_{0.65}\mathrm{Fe}_{0.35})\mathrm{O}$ (*Chen et al.*, 2012) and to FeO (this study).

3.2 X-ray Diffraction

The (Mg,Fe)O solid solution, excluding the end member FeO, is found in one of two crystal structures in the pressure and temperature range of studies that we conducted. In this chapter, at room pressure and temperature, $(\mathrm{Mg}_{0.06}\mathrm{Fe}_{0.94})\mathrm{O}$ is face-centered cubic, also referred to as $B1$ or rocksalt structure. Its space group is $Fm\text{-}3m$, and the first five reflections, i.e. first 3 lattice planes probed with increasing 2θ, are (111), (200), and (220), where the numbers (hkl) refer to the Miller indices of the lattice planes. In a cubic system, the spacing between lattice planes, or $d-$spacing, geometrically gives the lattice constant a:

$$d_{hkl} = \frac{a}{(h^2 + k^2 + l^2)^{1/2}} \tag{3.1}$$

At high pressure, between 8 and 40 GPa and depending on composition and hydrostatisticy of the sample environment, the cubic structure undergoes a distortion to a rhombohedral structure (space group $R\text{-}3m$). Rhombohedral unit cells are often described using a hexagonal coordinate system, which encompasses the rhombohedron (the c axis of the hexagonal cell corresponds to the long body-diagonal of the rhombohedral unit cell). In this description, the (111) reflection splits into two: (003) and (101), the (200) is renamed as the (012) reflection, and the cubic (220) splits into hexagonal (110) and (104).

X-ray diffraction is a scattering technique that measures the elastic, coherent scattering of X-rays off electrons (e.g. *Fultz and Howe*, 2008, and references therein). Powder XRD is variation of this technique that assumes that sampled grains are randomly oriented, such that scattering in the forward direction samples all allowed reflections. We apply this method to understand the changes in unit cell variations with pressure (and temperature, see Chapter 4).

X-ray diffraction can often be performed with in-house X-ray diffractometers with fixed-wavelength sources. The small sample size of diamond anvil cell experiments, however, require higher-intensity radiation to achieve reasonable experiment times. The high flux and versatile energy range of synchrotron experiments make them ideally suited for high pressure experiments. See *Duffy and Wang* (1998) for a discussion on performing high pressure and temperature XRD experiments at the synchrotron.

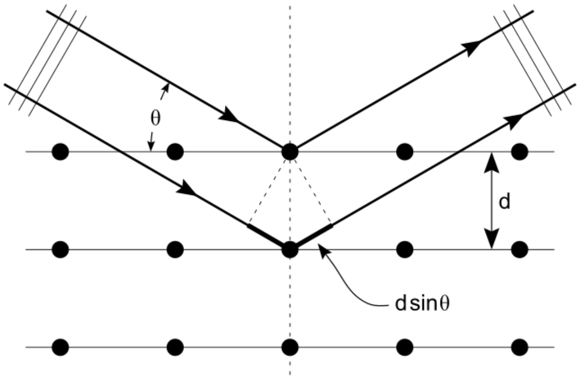

Figure 3.2: Illustration of Bragg's law in X-ray diffraction. Elastic scattering occurs in all directions, but constructive interference occurs in directions in which the Bragg condition is satisfied: $n\lambda = 2dsin\theta$.

The XRD measurements presented in this chapter were measured in conjunction with nuclear resonant scattering experiments at Sector 3-ID-B of the Advanced Photon Source, where a MAR345 image plate is inserted downstream from the sample. The angle-dispersive X-ray pattern is integrated radially using the Fit2D software (*Hammersley et al.*, 1996). A CeO_2 standard is used to calibrate both the X-ray beam center and the distance between the X-ray focus spot and the detector.

The wavelength is optimized, in these experiments, for the resonance energy of ^{57}Fe of 14.4125 meV. This energy, by design, is not optimized for XRD. The $\sim$ 1 meV bandwidth provides relatively small flux compared to beam lines tailored for XRD, and the scattering cross-section of electrons at this energy is small. As a result, typical XRD exposures of oxides in a diamond anvil cell require 10 minutes at low pressure and up to 30 minutes at high pressure, whereas at tailored beam lines for XRD at high pressure (e.g. 13-ID-D, APS) exposures are $\sim$ 1 minute to 2 minutes. Nevertheless, in-situ XRD is required for accurate sound velocity determinations from NRIXS measurements, as the pressure gradients (and therefore uncertainty in the absence of in-situ XRD) can reach upwards of 10 GPa across 100 μm.

3.3 Experimental Details

3.3.1 NRIXS with in-situ XRD

This high-pressure nuclear resonance scattering experiment was conducted at Sector 3-ID-B of the Advanced Photon Source at Argonne National Laboratory in August 2011 and October 2012. Three samples were prepared for this experiment. For the high pressure points, beveled anvils with 300 μm-culets were used. The $(Mg_{0.06}Fe_{0.94})O$ sample was embedded in boron epoxy, with rubies on either side, one on each culet. The pressure of the sample's environment was tracked with both ruby fluorescence (*Mao et al.*, 1986, only visible in compression to initial pressure point) and "diamond edge" Raman spectroscopy of diamond anvil culet (*Akahama and Kawamura*, 2006), but ultimately the pressure of the sample was determined with in-situ X-ray diffraction. The ambient pressure data point was taken in air. A low pressure data point (11.6 GPa) was taken of a sample loaded in a DAC with beveled 400 μm-culets, with beryllium gasket, and KCl pressure medium. We summarize the compression points measured in Table 3.1.

At each compression point, we collected a series of inelastic spectra, a synchrotron Mössbauer spectrum, and an X-ray diffraction spectrum (often both before and after the NRS spectra).

Raw spectra are shown in Figure 3.8. Energy scans were collected over a minimum energy range

	Environment	$P_{ruby}{}^{a}$ (GPa)	$P_{sample}{}^{b}$ (GPa)	Energy range (meV)	Scans, count times	$P_{XRD}{}^{c}$ (GPa)
1	air			$-80 \rightarrow +100$	1 at 3 sec/pt, 1 at 4 sec/pt	0
2	KCl, Be gasket		11.6	$-60 \rightarrow +70$	1 at 3 sec/pt, 5 at 5 sec/pt	$9.61(2)^{d}$
3	B epoxy	41.2	$43.5, 48.4^{e}$	$-60 \rightarrow +80$	1 at 3 sec/pt, 3 at 5 sec/pt	42.7(7)
4	B epoxy		59.1	$-60 \rightarrow +80$	1 at 3 sec/pt, 4 at 5 sec/pt	55(1)
5	B epoxy		$72, 76^{e}$	$-60 \rightarrow +80$	5 scans at 5 sec/pt	64(2)
6	B epoxy		85	$-60 \rightarrow +80$	7 scans at 5 sec/pt	81.6(7)
				$-70 \rightarrow +130$	1 at 3 sec/pt, 5 at 5 sec/pt	$81.1(8)^{f}$

Table 3.1: Details of the $(\mathrm{Mg_{0.06}Fe_{0.94}})\mathrm{O}$ NRIXS experiment. [a]Pressures were determined off-line using ruby fluorescence (*Mao et al.*, 1986). [b]Pressures were determined offline using the diamond edge (*Akahama and Kawamura*, 2006). [c]Pressures from XRD were determined from the combined equation of state of $(\mathrm{Mg_{0.06}Fe_{0.94}})\mathrm{O}$, given in Table 3.3 and Figure 3.5. [d]Number in parenthesis gives the error on the last digit. [e]Two numbers listed indicate before and after measurements [f]Without increasing pressure, the highest compression point was remeasured in October 2012.

of $-60 \rightarrow +70$ meV. At the highest compression point (#6, ~82 GPa), the energy scan was measured again in October 2012 with an extended energy range.

3.3.2 SMS with in-situ XRD

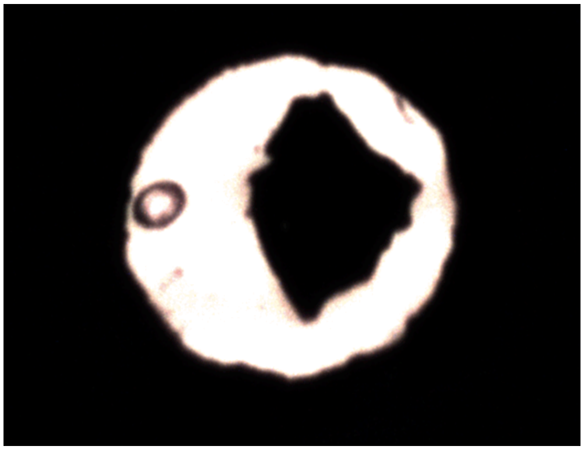

Figure 3.3: $(\mathrm{Mg_{0.06}Fe_{0.94}})\mathrm{O}$ at 50 GPa in the Synchrotron Mössbauer study. The sample chamber is 150 μm across. This study was conducted at 300 K. Ruby sphere is located to the left.

An independent synchrotron Mössbauer spectroscopy (SMS) experiment was carried out at Sector 3-ID-B of the Advanced Photon Source in February 2012. $(\mathrm{Mg_{0.06}Fe_{0.94}})\mathrm{O}$ was loaded in a diamond anvil cell with KCl as a pressure-transmitting medium in a rhenium metal gasket. A small ruby was included near the edge of the sample chamber (Figure 3.3). XRD and SMS were collected at 8 compression points over the range 7.8 to 52.4 GPa, determined by the equation of state of

KCl (*Dewaele et al.*, 2012). Ruby fluorescence was used to track the pressure offline. As Sector 3 is optimized for NRS (not XRD), with relatively low flux at a low energy with low scattering efficiency off electrons, we only observed one reflection of $(Mg_{0.06}Fe_{0.94})O$ (200) and KCl (110). One reflection is enough to determine the unit cell volume for cubic symmetry, which both KCl and $(Mg_{0.06}Fe_{0.94})O$ are at low pressure. At high pressure, we can estimate rhombohedral distortion, assuming that rhombohedral distortion is solely a function of pressure. In Chapter 4, Figure 4.8 shows the evolution of *d*-spacings as a function of pressure, and gives the interpolation $d_{012_R} \approx -0.0019 \times P + 2.1064$, a linear relationship between d-spacing of the rhombohedral (012) reflection and pressure. See Section 4.6 for more details.

The *d*-spacings and resulting pressure of KCl and $(Mg_{0.06}Fe_{0.94})O$ are summarized in Table 3.2. $(Mg_{0.06}Fe_{0.94})O$ d_{200} are interpreted as either cubic volumes or rhombohedral volumes.

P_{ruby} (GPa)	P_{KCl} (GPa)[a]	d_{110} KCl (Å)	d_{200} Mw94 (Å)	Vol/atom (Å^3)$_C$	Vol/atom (Å^3)$_R$
7.92	7.79	2.114	2.481	9.443	
11.72, 12.17	13.09	2.100	2.415	9.258	
15.71, 16.59	19.16	2.081	2.360	9.015	
19.71, 20.1	22.92	2.069	2.333	8.851	
23.84, 24.17	29.51	2.049	2.293	8.605	8.646
28.08, 28.62	35.73	2.036	2.262	8.439	8.487
34.97	43.47	2.018	2.228	8.223	8.275
	52.43	2.000	2.196	8.005	8.058

Table 3.2: XRD results of the $(Mg_{0.06}Fe_{0.94})O$ SMS experiment. When two numbers are listed, ruby pressures correspond to before and after the SMS and XRD measurement. [a]KCl pressure is determined from the *d*-spacing of KCl using the equation of state of KCl (*Dewaele et al.*, 2012). C and R subscripts indicate volumes assuming that the Mw94 *d*-spacing corresponds to the cubic (200) or rhombohedral (012) reflection.

3.4 Results

3.4.1 XRD: Isothermal Equation of State

A Birch-Murnaghan equation of state was fit to the pressure-volume data given in Table 3.2, given by the equations:

$$P(V) = 3K_0 f_E (1 + 2f_E)^{\frac{5}{2}} \left\{ 1 + \frac{3}{4}(K_0' - 4) f_E \right\} \tag{3.2}$$

$$f_E = \frac{1}{2}\left[\left(\frac{V_0}{V}\right)^{\frac{2}{3}} - 1\right] \tag{3.3}$$

where K_0 is the initial bulk modulus, K_0' is the pressure derivative of the bulk modulus, and f_E is Eulerian strain. K_0' fixed to 4. Pressure was determined by the equation of state of KCl (*Dewaele et al.*, 2012), and the results are summarized in Table 3.3. In the first fit, sample volumes were interpreted as being cubic given the measured d_{200} (Table 3.2). Cubic sample volumes are plotted as black circles in Figure 3.4. In the second fit, the rhombohedral estimates of volumes were included. These two fits are plotted in Figure 3.4.

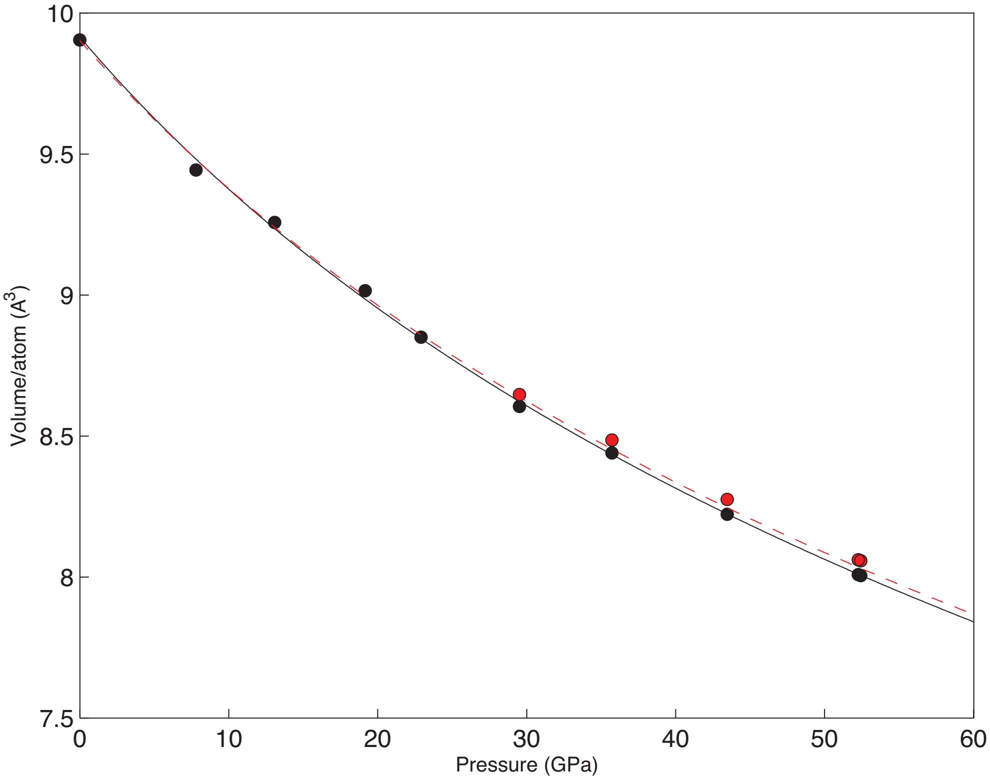

Figure 3.4: Volume of $(Mg_{0.06}Fe_{0.94})O$ at 300 K determined by its (200) reflection, with pressure determined by the volume of $B2$-KCl, determined by its (110) reflection, using the equation of state given by *Dewaele et al.* (2012). Black line is a Birch-Murnaghan equation of state with K_{0T}' fixed to 4, giving $V_0 = 9.91(2)$ Å^3/atom, $K_{0T} = 160(2)$ GPa. Red circles show volumes assuming a rhombohedral structure (See text and Table 3.2), and the red dashed curve shows the fit calculated with those points included ($V_0 = 9.90(3)$ Å^3/atom, $K_{0T} = 164(4)$ GPa). Equation of state results are summarized in Table 3.3.

In the third fit, the room temperature rhombohedral quench data from our high pressure and temperature XRD experiment (Chapter 4) are also included. We plot this combined equation of state in Figure 3.5. This equation of state is used to determine pressure in the NRIXS study.

	V_0 (Å^3)	K_{0T} (GPa)	K'_{0T}
Assume cubic	9.91(2)	160(2)	4 (fixed)
Include rhombo	9.90(3)	164(4)	4 (fixed)
Combined[a]	9.90446(*fixed*)	189(4)	2.9(1)

Table 3.3: Equations of state fit to the $(Mg_{0.06}Fe_{0.94})O$ dataset. [a]In this fit, the ambient temperature dataset was combined with the 300 K quench data of $(Mg_{0.06}Fe_{0.94})O$ from our high pressure and temperature XRD study (discussed in Chapter 4).

3.4.2 SMS: Magnetic Ordering Transition

Figure 3.6 shows the spectra from the synchrotron Mössbauer experiment. Pressure determined by the equation of state of KCl are shown on the right. At low pressure the spectra are characterized by slow oscillations, consistent with no magnetic ordering. With increasing pressure, it is expected that the quadrupole splitting of the nuclear excited state should increase as inter-atom bond shortening accentuates the intra-atom electric field gradient, i.e. the rate of change of electric field at the nucleus. This effect is reflected in the SMS spectrum in the shortening of period between 8 and 13 GPa. This trend does not persist at higher pressures. At 19 GPa the period in the SMS spectrum has increased and continues to do so with pressure up to 23 GPa. At higher pressure the spectra are characterized by fast, irregular oscillations, indicative of a magnetically-ordered state coupled with thickness effects.

The changes in the SMS spectrum preceding the magnetically-ordered state at 30 GPa are either indicative of a growing magnetically-ordered component, indicating a gradual transition, or some other change preceding a sharp transition. Careful fitting of the spectra is required.

In Figure 3.7, SMS spectra measured in-situ in the NRIXS experiment are shown. Pressures listed are determined from the combined equation of state of $(Mg_{0.06}Fe_{0.94})O$ (Table 3.3) using the

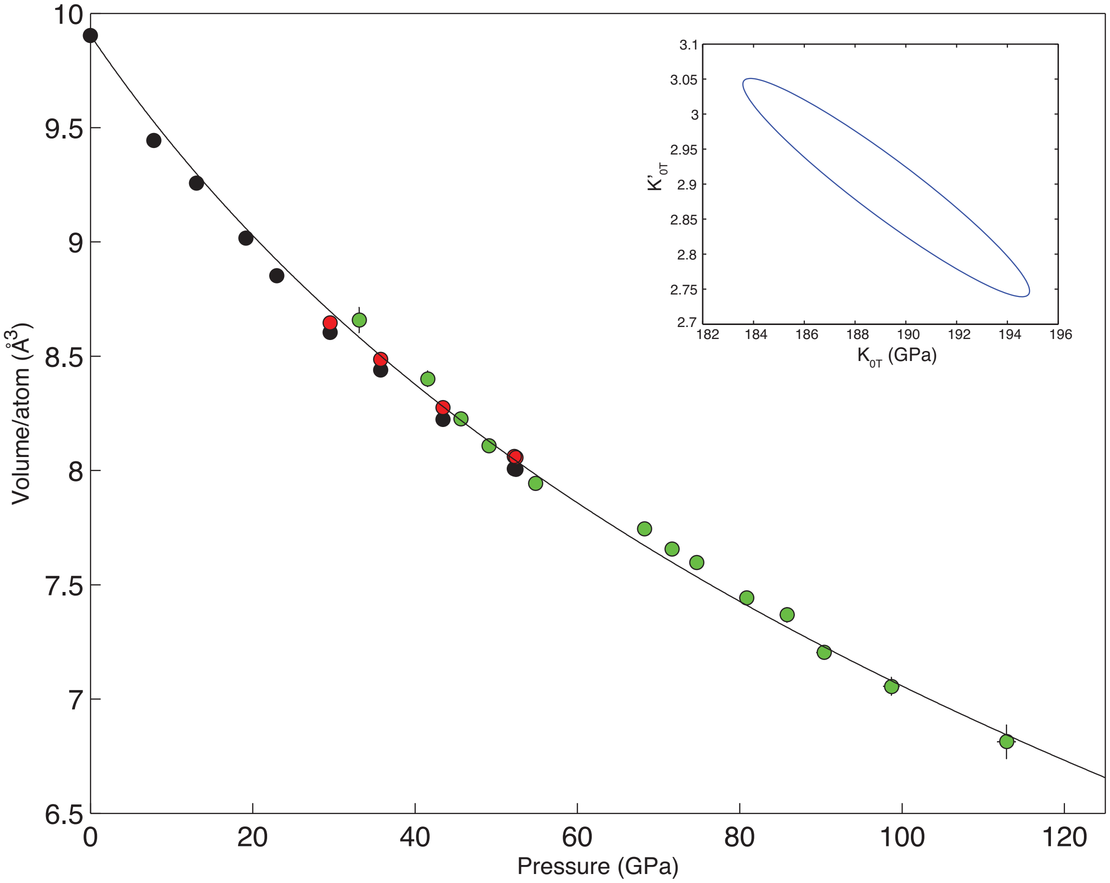

Figure 3.5: Volume of $(Mg_{0.06}Fe_{0.94})O$ measured in the SMS experiment (black and red circles, also shown in Figure 3.4) and the thermal equation of state study in Chapter 4. Green circles are volumes of rhombohedral "quench" points after each heating cycle of $(Mg_{0.06}Fe_{0.94})O$ in the buffered experiments, described in Section 4.6 and summarized in Table 4.6. The black line is a Birch-Murnaghan equation of state with $V_0 = 9.90446$ Å^3/atom (fixed), $K_{0T} = 189(4)$ GPa and $K'_{0T} = 2.9(1)$. Inset: 1σ error ellipse of K_{0T} and K'_{0T}.

d-spacings from in-situ XRD at each NRIXS pressure point (Table 3.4). Spectra were collected only over the pressure range 43-82 GPa, and all display magnetic ordering and thickness effects. As expected, there is no evidence of a spin transition in the pressure range probed by this study.

3.4.3 NRIXS: Sound Velocities

NRIXS spectra were collected over the pressure range 0 to 82 GPa. Raw spectra are shown in Figure 3.8. The phonon peak around 19 meV at ambient pressure moves out to about 24 meV at 55 GPa as vibrations move to higher energy with pressure. We see the emergence of the multi-phonon contribution to the vibrational spectrum at around 80 meV, most visible in the extended energy

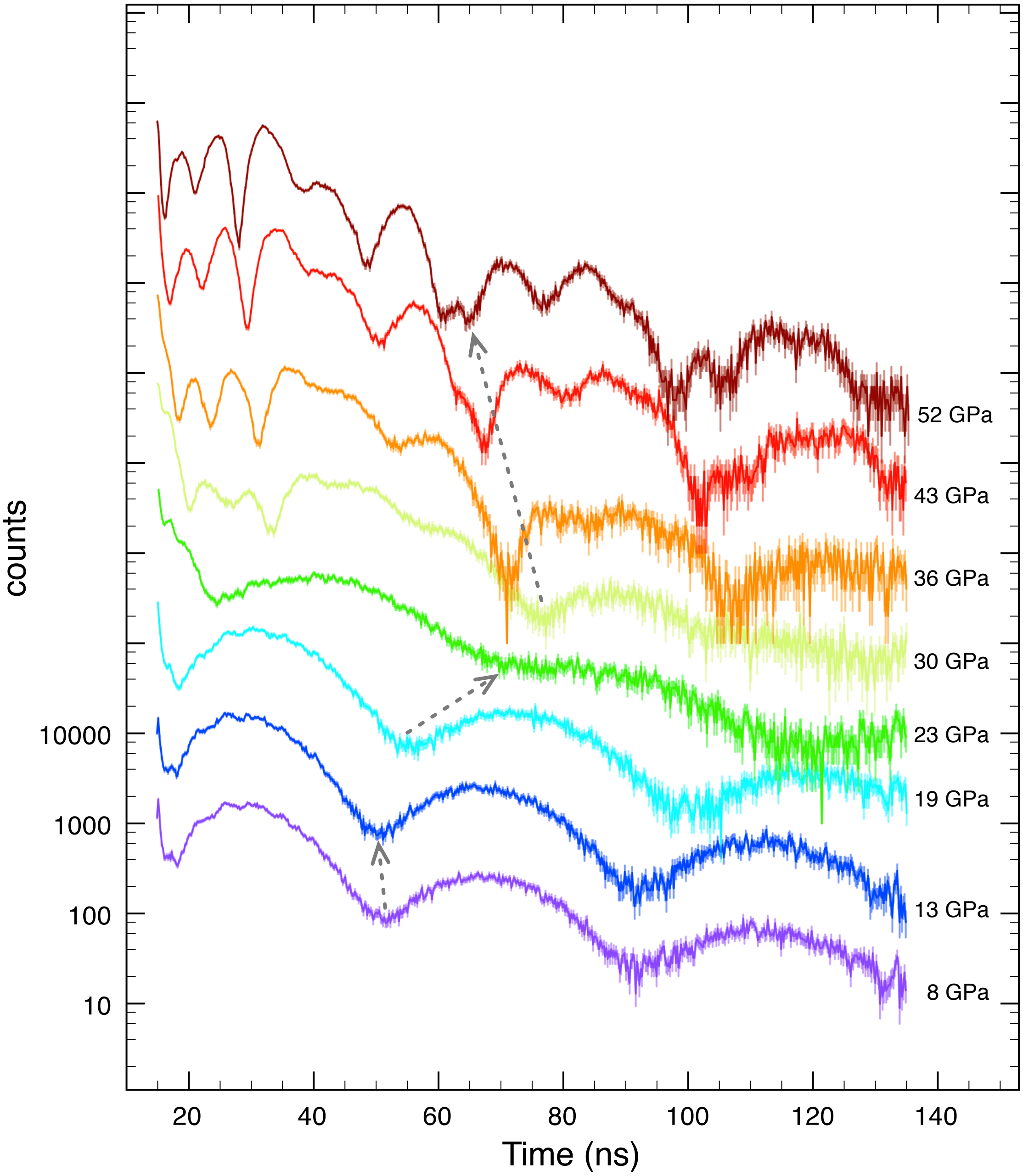

Figure 3.6: Synchrotron Mössbauer spectra of ($Mg_{0.06}Fe_{0.94}$)O at 300 K, with data binned into groups of 4. A magnetic transition occurs between 23 and 30 GPa. Pressures listed are determined from the equation of state of KCl (*Dewaele et al.*, 2012).

range of the 82 GPa pressure point.

Energy scans from our NRIXS study were processed using the PHOENIX software (*Sturhahn*, 2000) using methods described in *Sturhahn* (2004). Resulting PDOSs are shown in Figure 3.9.

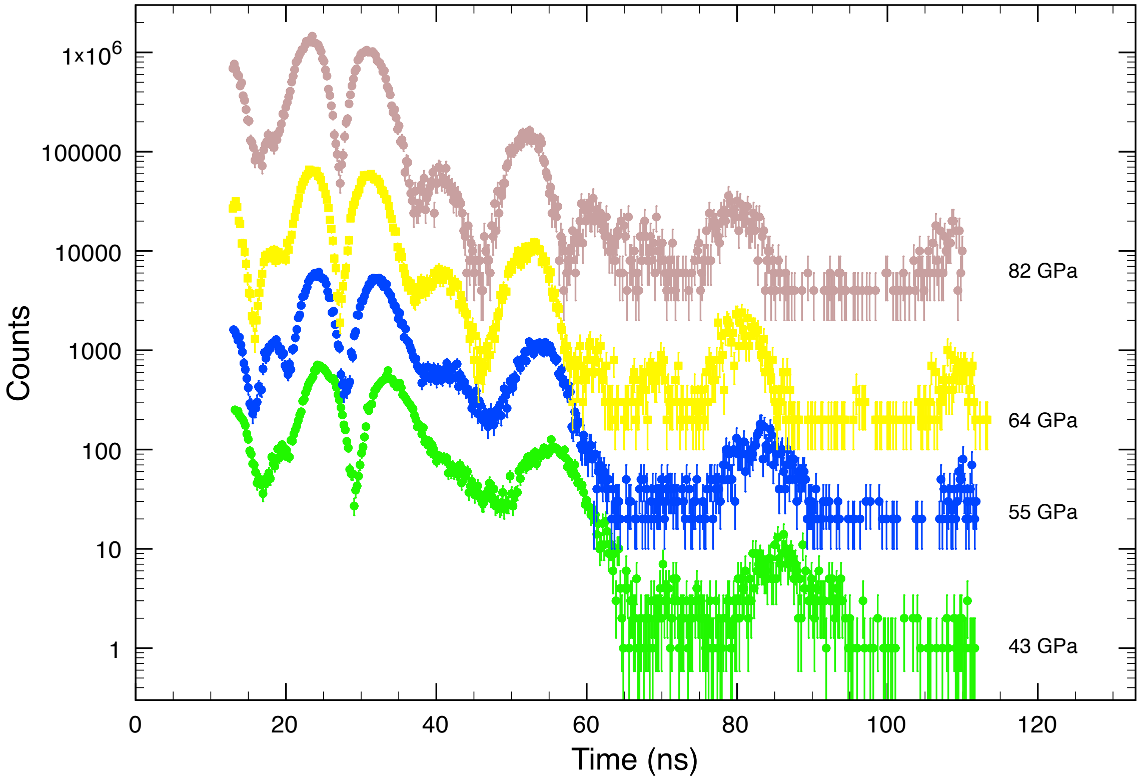

Figure 3.7: In-situ synchrotron Mössbauer spectra of $(Mg_{0.06}Fe_{0.94})O$ at 300 K, with data binned into groups of 4. A magnetic transition occurs between 23 and 30 GPa. Pressures listed are determined from the combined equation of state of $(Mg_{0.06}Fe_{0.94})O$, summarized in Table 3.3. The *d*-spacings from in-situ XRD used to calculate the pressure are listed in Table 3.4.

Figure 3.10 shows, in detail, two different phonon dispersion models applied to the low-energy region of the PDOS to derive the Debye velocity using the *psvl* subroutine in PHOENIX. In this procedure, the PDOS is scaled according to Equation 2.1. A strict "Debye-like" region varies quadratically with energy, which would be flat in this scaling (red line, Figure 3.10). More data can be included if we don't impose such a strict scaling, fitting instead an empirical function $f(E) \approx V_D \{1 - (E/E_0)^2\}$ that projects to zero energy (blue line, Figure 3.10). In either case, the zero-energy limit of the scaled PDOS is the Debye velocity (V_D). The lower energy limit of the fitting region to obtain this intercept is limited by the successful subtraction of the elastic peak. The upper limit of the fitting region is determined both by visual inspection, the χ^2 of fitting, and reasonable energy ranges where the phonons behave like an acoustic medium.

Results from fitting in the *psvl* routine are presented in Table 3.4 and Figure 3.11. Fitting with

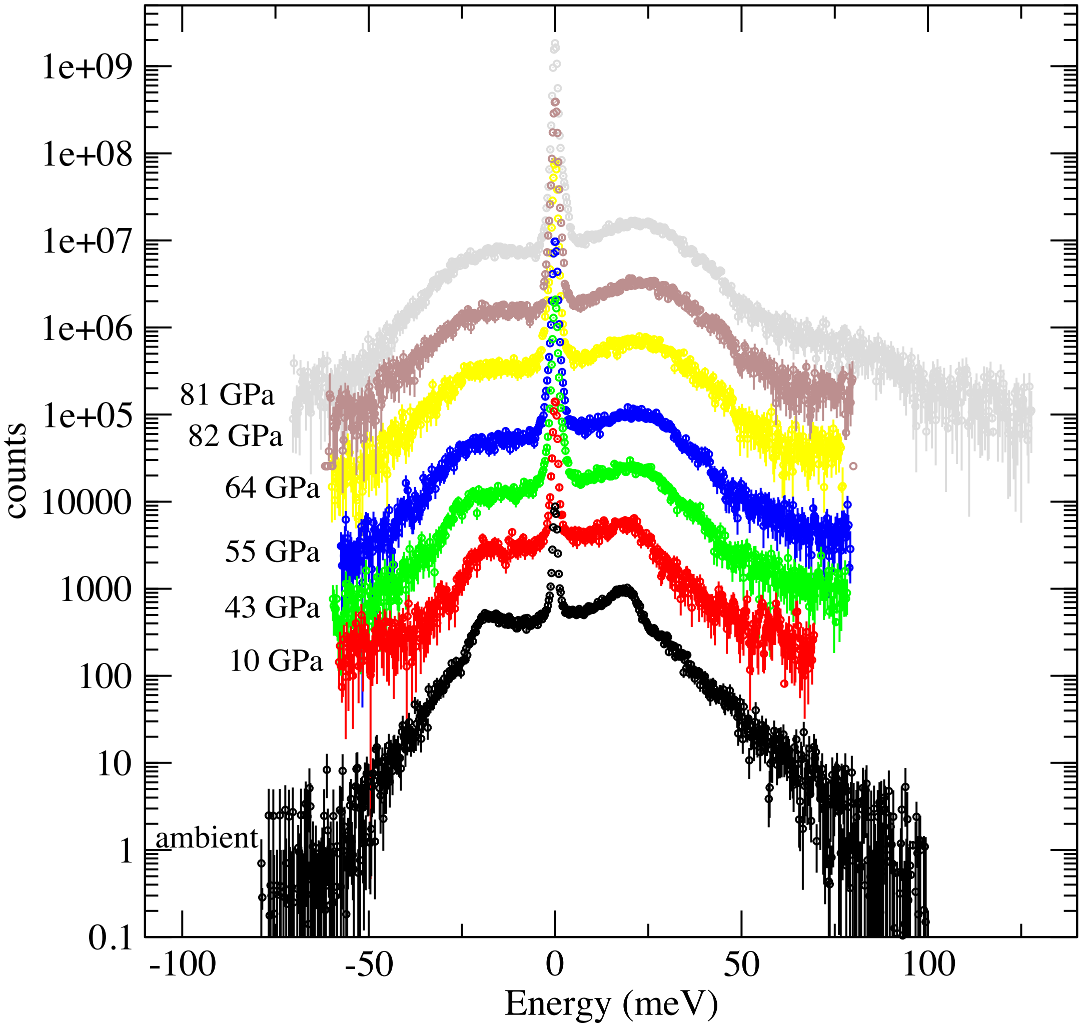

Figure 3.8: Raw NRIXS spectra of $(Mg_{0.06}Fe_{0.94})O$ at 300 K. Spectra are offset in the y-direction for clarity.

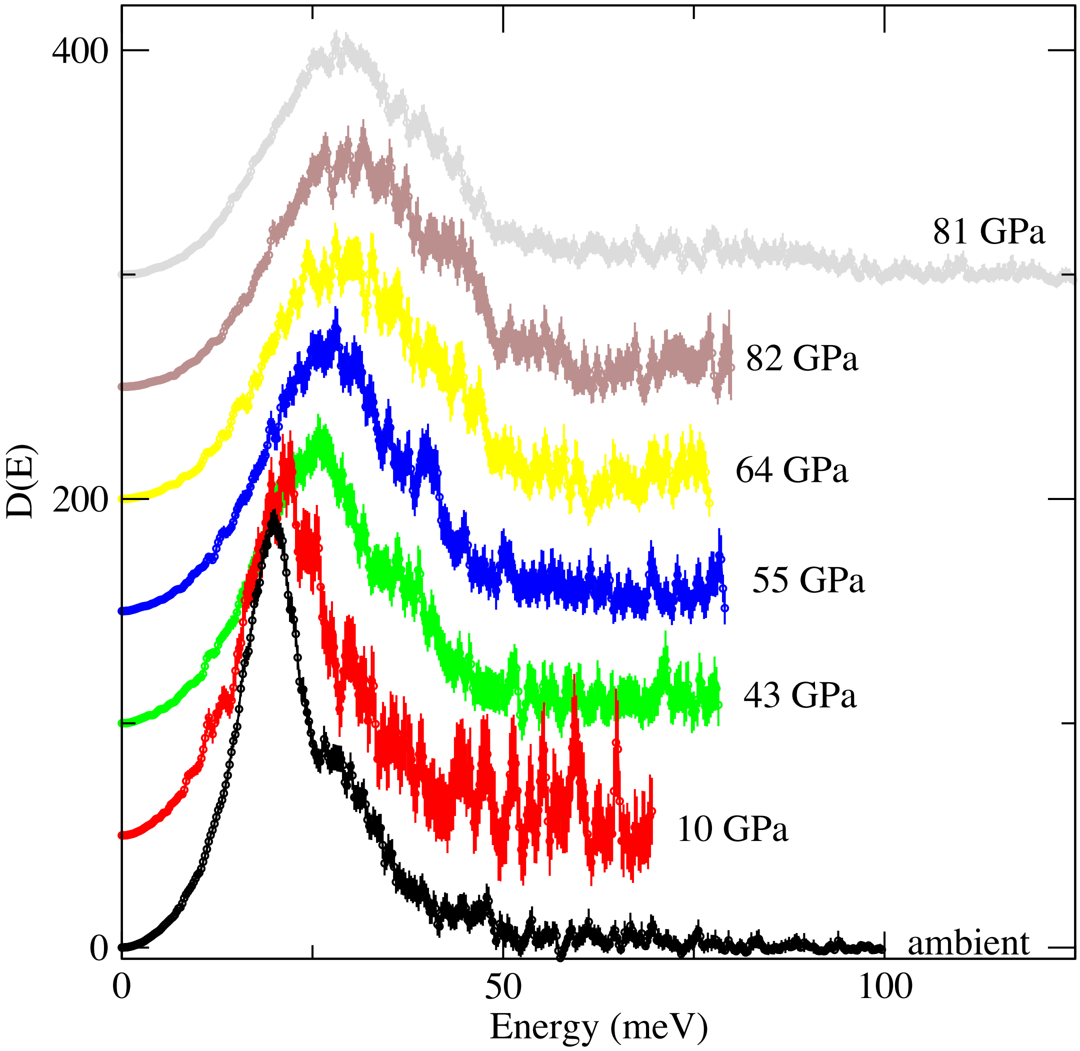

Figure 3.9: Partial projected phonon density of states of $(Mg_{0.06}Fe_{0.94})O$ at 300 K, extracted from raw spectra using PHOENIX (*Sturhahn*, 2000). Spectra are offset in the y-direction for clarity.

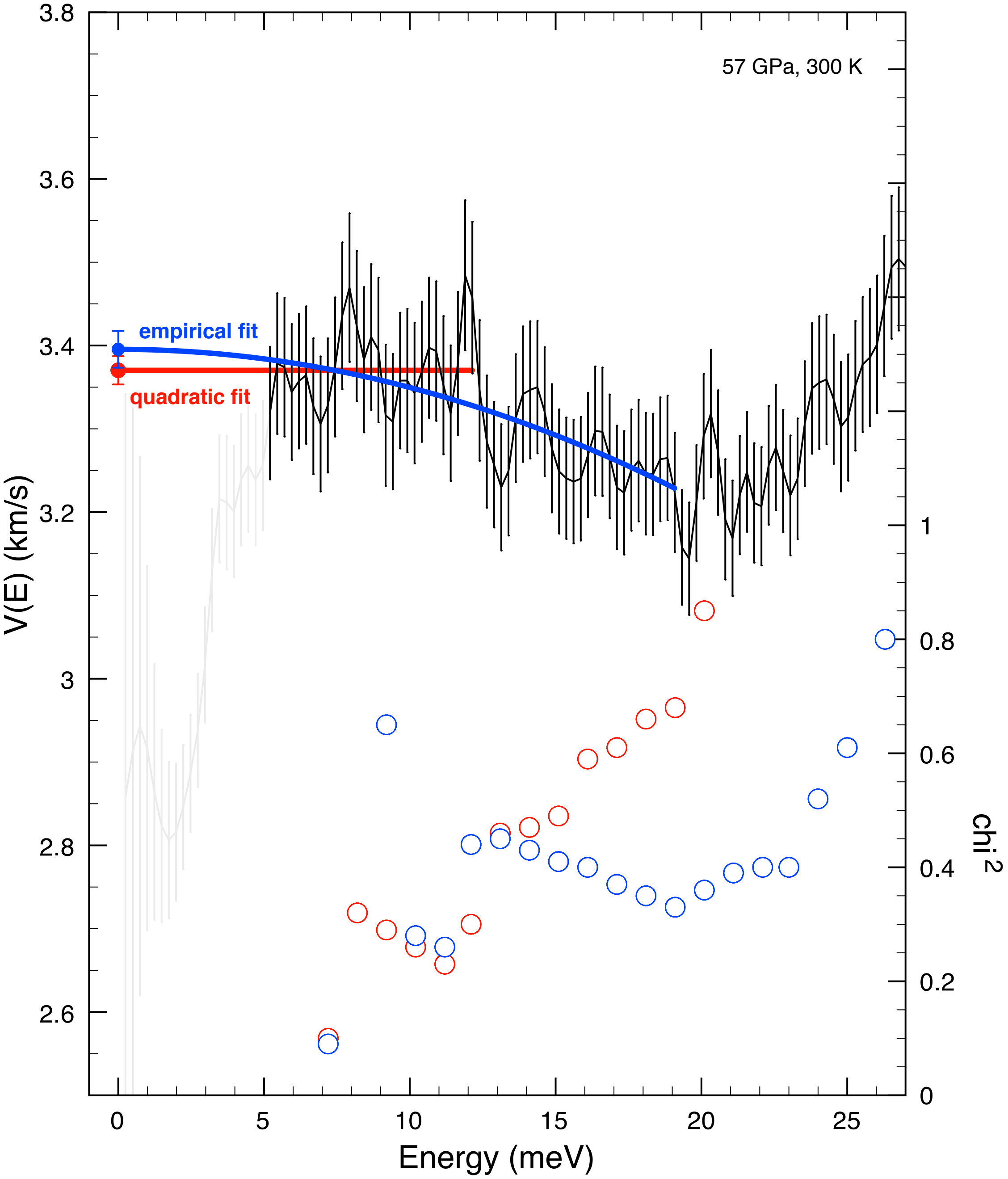

Figure 3.10: Debye velocity determination using the *psvl* subroutine in PHOENIX at 57 GPa. The PDOS is scaled according to Equation 2.1. A quadratic fit to $V(E)$ best describes data up to 12 meV (red line). More of the PDOS can be included if an empirical function is instead used (blue line). V$_D$ is the intercept at $E = 0$ (red and blue circles). Open circles are the χ^2 values calculated in *psvl*, plotted at the E_{max} of each calculation.

the quadratic requirement uses a smaller range of energy.

in-situ d_{200} (Å)	ρ (g/cc)	$V_{D(normal)}$ (km/s)	$E_{min} - E_{max(normal)}$ (meV)	$V_{D(quad)}$ (km/s)	$E_{max(quad)}$ (meV)
2.480^a	5.93(2)	3.08(1)	5.0 – 14.1		
2.114	6.23(3)	2.97(2)	5.7 – 19.9	2.94(2)	10.7
$2.023, 2.022^b$	7.08(4)	3.27(2)	5.7 – 18.6	3.25(2)	10.6
$1.998, 1.995^b$	7.36(4)	3.40(2)	5.2 – 19.1	3.3(2)	12.1
$1.980, 1.975^b$	7.58(4)	3.62(2)	3.7 – 20.8	3.59(2)	10.7
$1.948, 1.946^b$	7.95(3)	3.78(2)	5.9 – 21.0	3.69(2)	10.9
1.948	7.94(6)	3.73(2)	5.2 – 17.9	3.64(1)	9.0

Table 3.4: Debye Velocity (V_D) of $(Mg_{0.06}Fe_{0.94})O$ as a function of in-situ density, calculated with both the quadratic fit and normal fit. This data is shown in Figure 3.10. [a]This particular *d*-spacing corresponds to the (111) reflection. [b]Two *d*-spacings correspond to before and after XRD measurements.

Debye velocities of $(Mg_{0.06}Fe_{0.94})O$ are compared to those of $(Mg_{0.65}Fe_{0.35})O$ (*Chen et al.*, 2012) and FeO (this study, Appendix A.3) in Figure 3.12. In this plot, the $(Mg_{0.06}Fe_{0.94})O$ and $(Mg_{0.65}Fe_{0.35})O$ densities were determined with in-situ XRD. The densities for FeO at low pressure was determined by volume measured with XRD at Sector 12.2.2 of the Advanced Light Source, and at high pressure by volume measured with XRD at Sector 13-ID-D, GSECARS in February 2012.

Using the combined equation of state determined in Section 3.4.1, shown in Figure 3.5, we calculated pressure from our in-situ densities and the seismically relevant V_P and V_S from our V_D. The results are summarized in Table 3.5. In Figure 3.13, we plot V_P and V_S as a function of pressure. For comparison, we plot the sound velocities of $(Mg_{0.65}Fe_{0.35})O$, measured using NRIXS with in-situ XRD by *Chen et al.* (2012). At 70 GPa, $(Mg_{0.65}Fe_{0.35})O$ is just coming out of a spin transition, which is reflected in the low P-wave velocities. Between 100 and 140 GPa, the sound velocities of $(Mg_{0.65}Fe_{0.35})O$ are linear with pressure. $(Mg_{0.65}Fe_{0.35})O$ is more iron-rich than expected for typical lower mantle ferropericlase (*Murakami et al.*, 2005), and could be present in in iron-enriched regions of the lower mantle. The sound velocities of $(Mg_{0.06}Fe_{0.94})O$ are much lower than those of $(Mg_{0.65}Fe_{0.35})O$, and better able to explain ULVZs.

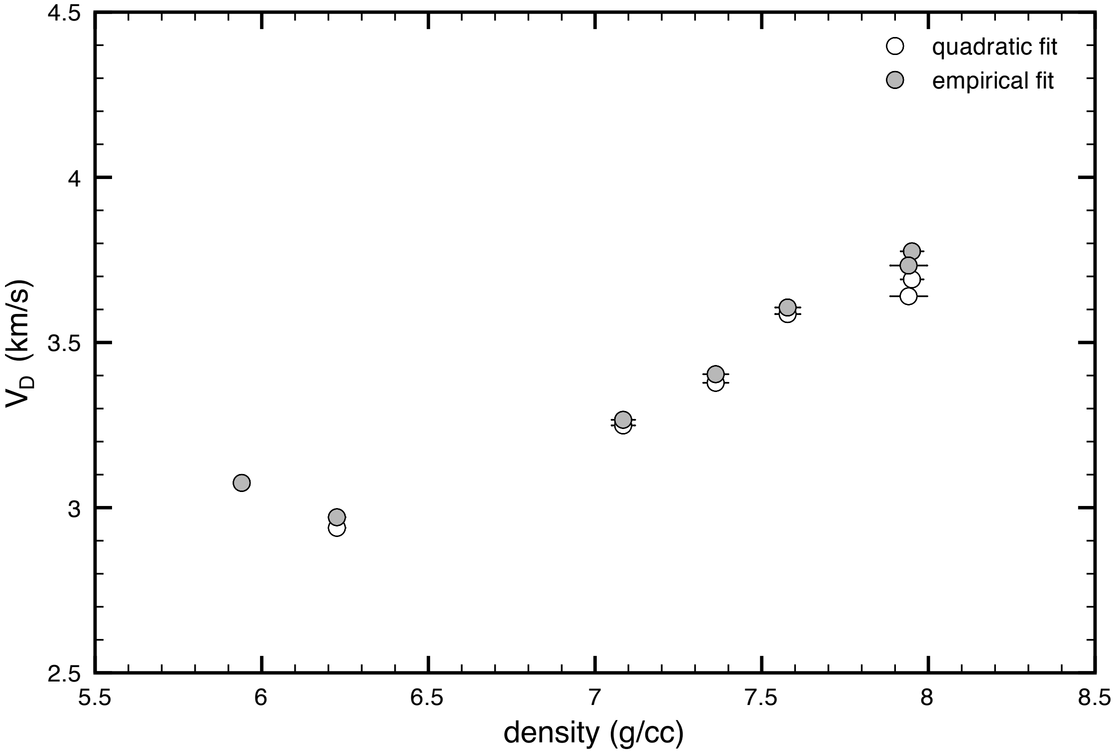

Figure 3.11: Debye velocity (V_D) of ($Mg_{0.06}Fe_{0.94}$)O at 300 K as a function of density. Fits in which a quadratic form of the low-energy region of the PDOS is assumed are shown in white, while a more flexible parameterization of the low-energy region results in Debye velocities shown in gray (empirical fit), as described in the text. Figure 3.10 illustrates the difference between the two fitting routines.

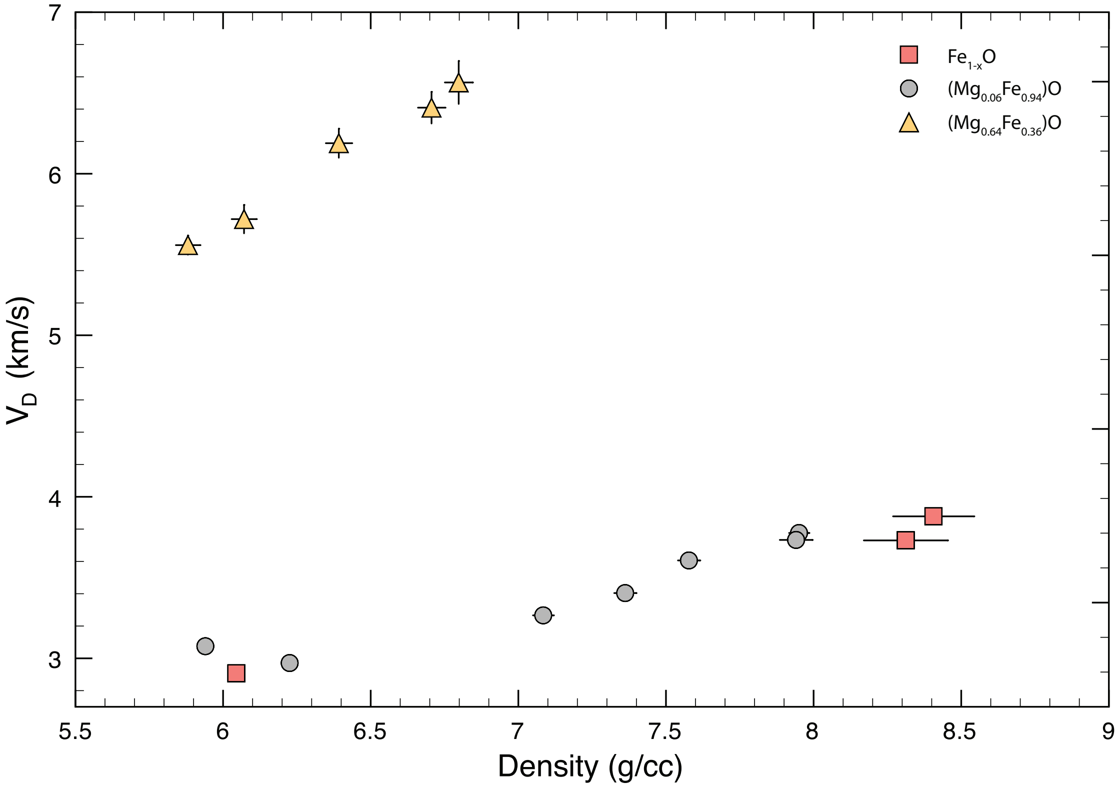

Figure 3.12: (V_D) of $(Mg_{0.06}Fe_{0.94})O$ compared to FeO (Section A.3) and $(Mg_{0.65}Fe_{0.35})O$ (*Chen et al.*, 2012) at 300 K, as a function of in-situ density. $(Mg_{0.65}Fe_{0.35})O$ and $(Mg_{0.06}Fe_{0.94})O$ volumes were measured in-situ at Sector 3-ID-B of the Advanced Photon Source (APS). The volumes of FeO were measured at Sector 12.2.2 of the Advanced Light Source (low density) and at Sector 13-ID-D of the APS (high density). $(Mg_{0.16}Fe_{0.84})O$ is not included in this figure as its volume was not measured in-situ at either Sector 3-ID-B or Sector 13-ID-D.

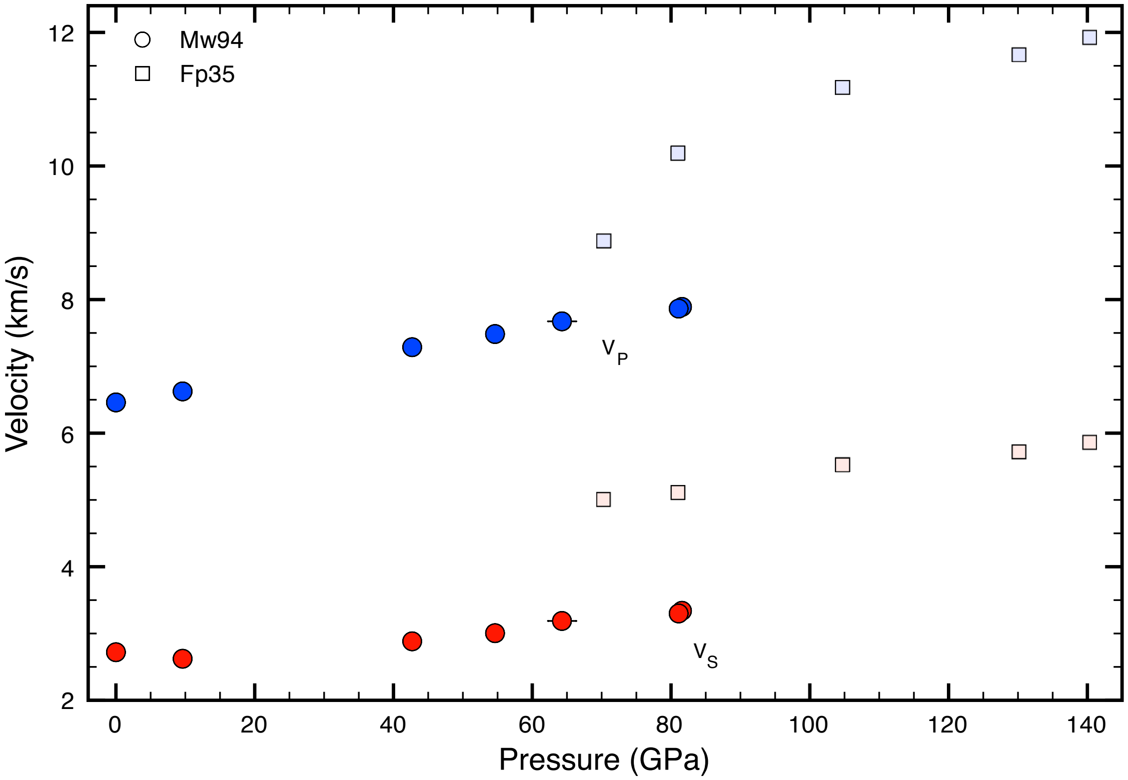

Figure 3.13: Compressional (V_P, red) and shear (V_S, blue) wave velocities of $(Mg_{0.06}Fe_{0.94})O$ at 300 K, over the pressure range 0 to 82 GPa (circles). For comparison, the velocities of $(Mg_{0.65}Fe_{0.35})O$ are shown as light blue and red squares(*Chen et al.*, 2012).

$\rho^{a,b}$ (g/cc)	Pressure^c (GPa)	V_D (km/s)	V_P (km/s)	V_S (km/s)	G (GPa)	K (GPa)
5.93(2)	0	3.08(1)	6.47(5)	2.72(1)	43.9(4)	189(3)
6.23(3)	9.61(2)	2.97(2)	6.63(6)	2.62(2)	42.8(7)	216(4)
7.08(4)	42.7(7)	3.27(2)	7.29(8)	2.88(2)	58.9(8)	288(7)
7.36(4)	55(1)	3.40(2)	7.48(8)	3.01(2)	66.5(9)	324(8)
7.58(4)	64(2)	3.61(2)	7.67(8)	3.19(2)	77.0(9)	344(8)
7.95(3)	81.6(7)	3.78(2)	7.89(9)	3.34(2)	89(1)	377(9)
7.94(6)	81.1(8)	3.73(2)	7.87(9)	3.30(2)	86.5(8)	376(9)

Table 3.5: Summary of sound velocities and bulk and shear moduli of $(Mg_{0.06}Fe_{0.94})O$ as a function of pressure. V_P and V_S are shown in Figure 3.13. ^{a} Number in parenthesis is the error on the last digit. ^{b}From Table 3.4. ^{c}Pressure is determined from the equation of state of $(Mg_{0.06}Fe_{0.94})O$, summarized in Table 3.3.